Electrical Impedance Tomography Image Reconstruction using Convolutional Neural Network with Periodic Padding

Guilherme C. Duran [*,1] **André K. Sato** [*,2] **Edson K. Ueda** [*,3]
Rogério Y. Takimoto [*,4] **Thiago C. Martins** [*,5]
Marcos S. G. Tsuzuki [*,6]

[*] *Laboratory of Computational Geometry*
Mechatronics and Mechanical Systems Engineering Department,
Escola Politécnica da Universidade de São Paulo, São Paulo, Brazil

Abstract: Electrical Impedance Tomography (EIT) is a noninvasive, indirect image reconstruction technique which consists in the inference of the distribution of electrical conductivity inside a body or object from the set of electrical potentials measured on its boundary. Several methods have been used for the reconstruction of EIT images, such as Simulated Annealing, Kalman Filter, D-bar, and, more recently, Convolutional Neural Networks (CNN). An issue when using CNN is that the resulting image of the convolution process is smaller than the original input image. Besides that, the values lying on the borders of the input image are used less, hence their importance is overlooked. This problem is usually addressed by the introduction of padding, which is the addition of layers in the borders of the original input image. This work proposes the use of a doubly periodic padding, which is relevant for toroidal image problems such as the electric potential distribution measured using EIT. The CNN is trained using a database generated by numerical simulations. The resulting image reconstructions are presented for different noisy potential inputs.

Keywords: Electrical impedance tomography, Convolution neural networks, Periodic padding.

1. INTRODUCTION

Electrical Impedance Tomography (EIT) is a noninvasive, indirect method of image reconstruction. The technique consists in the inference of the distribution of electrical conductivity inside a body or object, which is done from the set of electrical potential values measured on its boundary.

EIT presents some advantages over other noninvasive methods, such as the fact that it does not depend on the emission of radiation and that the equipment used can be small and portable, with a relatively low cost. For these reasons, EIT has been used in several applications, including the real-time monitoring of industrial processes and biomedical analysis (Martins et al., 2011; Silva et al., 2017).

Among the applications of the EIT, those in the medical field stand out. EIT can be used for the continuous observation of pulmonary function to instantly assess the effects of therapeutic maneuvers on the regional distribution of ventilation (Teschner et al., 2015), as well as for the diagnosis of pulmonary embolism, detection of tumors in the chest area and diagnosis and distinction of ischemic and hemorrhagic stroke (Lymperopoulos et al., 2017).

The EIT equipment responsible for data acquisition is an electrode belt. Once the belt is positioned around the body or object studied, a low amplitude current pattern is applied through a pair of electrodes, and then the electrical potentials resulting from such application are measured along the contour of the domain. Then, the current pattern is changed, that is, the current is applied through another pair of electrodes and the potentials are measured again, and so on, to obtain a large amount of electrical potential data for a given conductivity distribution.

The aforementioned procedure in presented in Fig. 1. A current pattern J_i, $i \in [1, 32]$ is applied to a domain with conductivity distribution $\sigma(x, y)$. For each current injection, the electrical potential Φ_j^i, $j \in [1, 32]$ is measured relative to ground. In a 32-electrode configuration, it is possible to obtain up to 1024 potential values.

EIT can be used to reconstruct either differential or absolute images. The reconstruction of absolute images is substantially more difficult, and, until recently, clinically impracticable (Martins and Tsuzuki, 2012). The quality of reconstruction of absolute images is limited by the difficulty of solving the inverse problem, whereas neither the exact geometry of the object's contour nor the exact

[1] e-mail: guiduran@usp.br.
[2] e-mail: andre.kubagawa@gmail.com.
[3] e-mail: ueda.edson@gmail.com.
[4] e-mail: takimotoyugo@gmail.com.
[5] e-mail: thiago@usp.br.
[6] e-mail: mtsuzuki@usp.br.

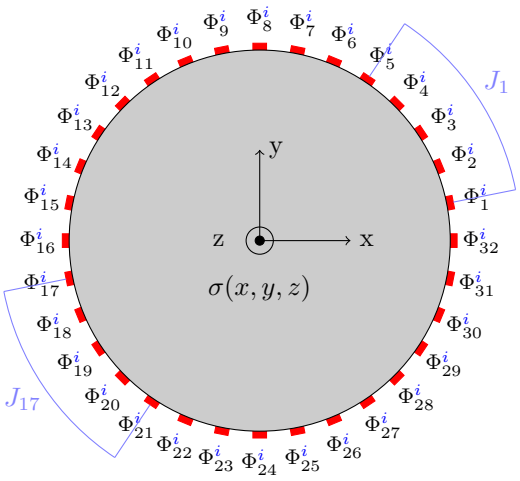

Fig. 1. For a given current pattern J_i, the set of electrical potential Φ^i_j, $j \in [1, 32]$ is measured relative to ground. This figure presents the scheme for injection of current patterns J_1 and J_{17}, each one skipping three electrodes.

arrangement of the electrodes on the surface are known. These limitations, together with low spatial resolution, make it difficult to implement EIT in clinical practice. However, the development of fast and robust reconstruction methods, as well as efficient data acquisition equipment, promoted the advancement and diffusion of the technique.

Several methods have been used for the reconstruction of EIT images, for instance, simulated annealing (Martins and Tsuzuki, 2011, 2013, 2015; Tavares et al., 2012, 2014, 2015; Martins et al., 2014; Sato et al., 2018), Kalman filter (Trigo et al., 2004) and D-Bar (Alsaker and Mueller, 2018). Recently, artificial neural network methods have also been used for solving and improving EIT reconstructions. Tan et al. (2018) and Bianchessi et al. (2020) used the LeNet Convolutional Neural Network (CNN) (Lecun et al., 1998) to solve the EIT inverse problem, while Hamilton and Hauptmann (2018) used a convolutional neural network for postprocessing direct reconstructions obtained with the D-bar method.

The main step of data processing in a convolutional neural network is the convolution itself. For a given $n \times n$ pixels input image, the output image resulting from a convolution using a filter of size $s \times s$ will be $(n-s+1) \times (n-s+1)$, that is, the resulting image size is smaller than the original one. Besides that, the values lying on the borders of the input image are used less, hence their importance is diminished. This problem is usually addressed by the introduction of padding, which is the addition of layers on the borders of the original input image. This work proposes the use of a doubly periodic padding, which is relevant in toroidal-like input image problems such as the electric potential distribution measured using EIT.

This paper is structured in the following way: Section 2 presents the convolutional neural network topology and the proposed modification of padding for toroidal mapping. In Section 3, the methodology used to generate training data for the artificial neural network is discussed. The reconstruction of a test set is displayed in Section 4 and, finally, the conclusion is presented in Section 5.

2. MODELLING THE EIT INVERSE PROBLEM USING A CONVOLUTIONAL NEURAL NETWORK

Solving the inverse problem of EIT with artificial neural networks (ANN) means training a model which takes as input the set of electrical potentials measured on the boundary of the body and outputs an associated conductivity map.

A CNN, a special kind of ANN, consists of convolution, activation, and pooling. In the convolution step, filters move across the images to recognize patterns in the input data. This is done by multiplying the kernel F, indexed from -N to N, by the overlapping input image area,

$$F * I(x, y) = \sum_{j=-N}^{N} \sum_{i=-N}^{N} F(i, j) I(x - i, y - j) \qquad (1)$$

The resultant sum value is then assigned to the current pixel of the resulting convoluted image. After the convolution, an activation function is applied to each value of the resulting image.

Given the fact that the size of the filter side is always greater than one, the resulting image shrinks every time a convolution operation is performed. To bypass this problem, padding is usually applied, which adds layers to the borders of the original input image, so that the output remains of the same size. A typical padding is the zero (or "same") padding, which adds zeros to the borders. (Fig. 2).

0	0	0	0	**0**
0	1	2	3	0
0	4	5	6	0
0	7	8	9	0
0	0	0	0	**0**

Fig. 2. Zero padding layers added to the original image.

In this work, the potential vector of 1024 measurements is reshaped into a matrix of shape 32×32, where the rows corresponds to each current pattern and the columns to each electrode measurement. Then, the input data can be thought as an image. Besides that, the closed electrode belt suggests that there is a strong correlation between the first and the last columns of this matrix. Moreover, the first and last rows are correlated, as they represent neighboring current patterns injected in the domain. Therefore, the input can be seen as a toroidal-like image. This paper proposes the use of a doubly periodic padding for such a problem, as represented in Fig. 3.

After the activation, there is a pooling step, where a filter is applied to nonoverlapping subregions of the initial representation, replacing its value with a single value encountered inside the filter region. This is done to prevent overfitting the training data. When the replacing value is

9	7	8	9	7
3	1	2	3	1
6	4	5	6	4
9	7	8	9	7
3	1	2	3	1

Fig. 3. Doubly periodic padding layers added to the original image.

the maximum value within the filter region, the method is called *MaxPooling*.

The LeNet-5 network architecture was used in this work. Some modifications were made to adapt it to the regression problem covered herein, such as the adequacy of the number of neurons in the output layer. Another change concerns the use of a non-saturating activation function (Krizhevsky et al., 2012).

The topology of the CNN consists of:

(1) input layer, which contains data from 32 electrodes in 32 current applications;
(2) convolution layer with 30 filters of size 5×5, activation function *ReLU*, strides of 2×2 and *doubly periodic padding*;
(3) *maxPooling* layer with filters of size 2×2, stride of 2×2 and *zero padding*;
(4) second convolution layer, similar to the first, but with 240 filters;
(5) output layer with activation function *ReLU*, which has the number of neurons equal to the number of nodes in the reconstruction mesh.

The output dimension of each layer is shown in Fig. 4.

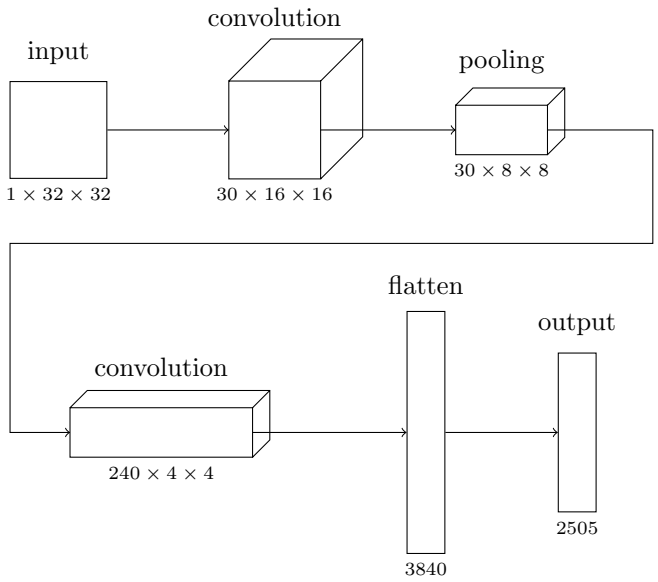

Fig. 4. The output dimension of each CNN layer.

3. ON THE GENERATION OF SYNTHETIC TRAINING DATA

Experimental EIT data is not widely available. Therefore, the generation of synthetic databases from numerical simulations is usually performed for obtaining large training sets.

From conductivity distributions generated synthetically, it is possible to estimate the electrical potentials resulting from the application of a current pattern using the forward formulation of the problem. Then, this data can be used to train the CNN. The framework for the generation of synthetic data was previously presented by the Authors (Duran et al., 2021).

The simulated data was generated in the following way:

(1) generation of a 2D mesh of radius $0.15m$ to represent the expected domain of the experiment;
(2) definition of a feasible random layout based on the geometry of the phantoms;
(3) definition of the conductivity distribution in the mesh nodes, given the layout of the phantoms and the conductivity of of each entity;
(4) solution of the forward problem using the Finite Element Method (FEM).

The EIT forward problem and the FEM are described in the following subsections.

3.1 The EIT forward problem

The frequencies of the currents applied in EIT are low enough so that the capacitive and inductive effects can be ignored. Under this hypothesis, the two-dimensional problem of EIT consists in solving the Laplace equation

$$\nabla \cdot (\sigma(x,y)\nabla\Phi(x,y)) = 0 \qquad (x,y) \in \Omega \tag{2}$$

where, $\sigma(x,y)$ and Φ are the conductivity and potential distributions, respectively, and Ω is the problem domain. The null result means that there are no current sources within the domain, what is expected in EIT (Martins and Tsuzuki, 2015; Martins et al., 2014). The forward problem of the EIT is defined as the determination of the distribution of electric potentials Φ over Ω.

Neumann boundary conditions are applied to the boundary

$$\sigma\frac{\partial\Phi}{\partial\hat{n}} = J \tag{3}$$

where $\hat{n}$ is the unit normal vector.

The analytical solutions for 3 and 2 for arbitrary domains are not available. An approximate solution can be obtained using the FEM.

3.2 Finite element formulation of the forward problem

FEM is a popular technique for modeling EIT forward problems. Using FEM, it is possible to approximate the equations of the problem to enable the solution for each

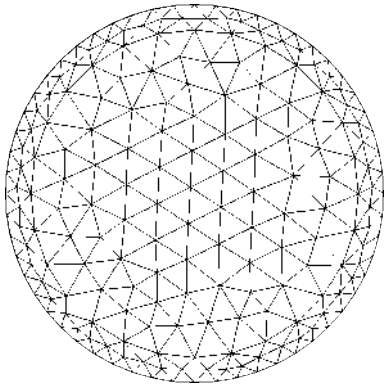

Fig. 5. An example of a mesh.

element of the mesh (see Fig 5). The accuracy of the method is controlled by the size of the element.

A triangular element was chosen for the FEM model, and a linear polynomial interpolation is adopted to determine the potential throughout the element. In this way, the element's conductance matrix, calculated using the notation shown in Fig. 6, can be described as

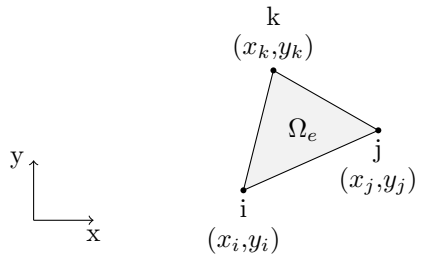

Fig. 6. Triangular element with nodes i, j and k.

$$
\begin{aligned}
[K]_e =& \sigma_e [BC]_e^T [BC]_e \int_{S_e} dxdy \\
=& \frac{\sigma_e}{4S} \begin{bmatrix} b_i & c_i \\ b_j & c_j \\ b_k & c_k \end{bmatrix} \begin{bmatrix} b_i & b_j & b_k \\ c_i & c_j & c_k \end{bmatrix} \\
=& \frac{\sigma_e}{4S} \begin{bmatrix} b_i^2 + c_i^2 & b_i b_j + c_i c_j & b_i b_k + c_i c_k \\ b_j b_i + c_j c_i & b_j^2 + c_j^2 & b_j b_k + c_j c_k \\ b_k b_i + c_i c_k & b_k b_j + c_k c_j & b_k^2 + c_k^2 \end{bmatrix},
\end{aligned} \tag{4}
$$

where,

$$
\begin{aligned}
&a_i = x_j y_k - x_k y_j \;\; a_j = x_k y_i - x_i y_k \;\; a_k = x_i y_j - x_i y_j \\
&b_i = y_j - y_k \;\; b_j = y_k - y_i \;\; b_k = y_i - y_j \\
&c_i = x_k - x_j \;\; c_j = x_i - x_k \;\; c_k = x_j - x_i.
\end{aligned} \tag{5}
$$

The local matrix of element $[K]_e$ must be computed for all elements of the mesh. Then, it should be assembled, generating a global conductance matrix K. The solution of the EIT forward problem using FEM is reduced to the solution of a linear system of equations

$$K \cdot \phi = J \tag{6}$$

where, J is the vector of currents and ϕ is the vector of potentials to be calculated.

4. RESULTS

The experiment was carried out with a layout containing the following phantoms:

- a circle of radius $0.03m$ and conductivity $0.005\ (\Omega \cdot m)^{-1}$;
- an equilateral triangle of side $0.06m$ and conductivity $0.005\ (\Omega \cdot m)^{-1}$;
- a square of side $0.06m$ and conductivity $0.005\ (\Omega \cdot m)^{-1}$.

The conductivity of the medium was set to $0.3815(\Omega \cdot m)^{-1}$, and current amplitude equals to $1.9mA$. In all, 30,000 training data were generated with the simulated experiments described above.

The hyperparameters used in the training were:

(1) batch size of 100 samples;
(2) number of epochs equals to 50;
(3) a validation dataset of 20% of training data;
(4) early stopping activated;
(5) Adam optimizer; and
(6) mean squared error loss function.

An additional set of 4 test conductivities was created for the visual evaluation of the reconstruction. For the test reconstruction, an electrical noise with normal distribution was added to the potential vector,

$$\chi \sim \mathcal{N}(0, \sigma^2), \qquad \sigma = \xi \cdot \max_{1 \le i \le 32} \phi_i \tag{7}$$

where ξ is a percentage applied to the maximum potential computed on each conductivity distribution. Three different percentages were applied to the test conductivities: 0, 1, and 2%.

Fig. 7, shows the reconstruction for each different noisy data, for the first two test layouts. It can be observed that when there is no electrical noise added to the potential vector (row number two, $\xi = 0$), reconstruction presents high contrast, especially for those phantoms positioned closer to the boundary and further apart from each other. As soon as the electrical noise raises from 1 to 2% (rows 3 and 4, respectively), the quality of CNN reconstructions worsen dramatically.

Likewise, Fig. 8 shows the reconstruction for the last two test layouts. These reconstructions show the same behavior of Fig. 7.

The mean quadratic errors in the test set were

- $3.1 \cdot 10^{-3}$, for $\xi = 0\%$;
- $9.8 \cdot 10^{-3}$, for $\xi = 1\%$;
- $18.1 \cdot 10^{-3}$, for $\xi = 2\%$.

5. CONCLUSION AND FUTURE WORK

In this work, a CNN-based solution to the 2D problem of Electrical Impedance Tomography was proposed using doubly periodic padding. The test set data proved good quality reconstruction for low noisy potential data (note that the proposed CNN was trained with noiseless data).

In the finite element model adopted here, only the real part of the electrical impedance was considered. The capacitive

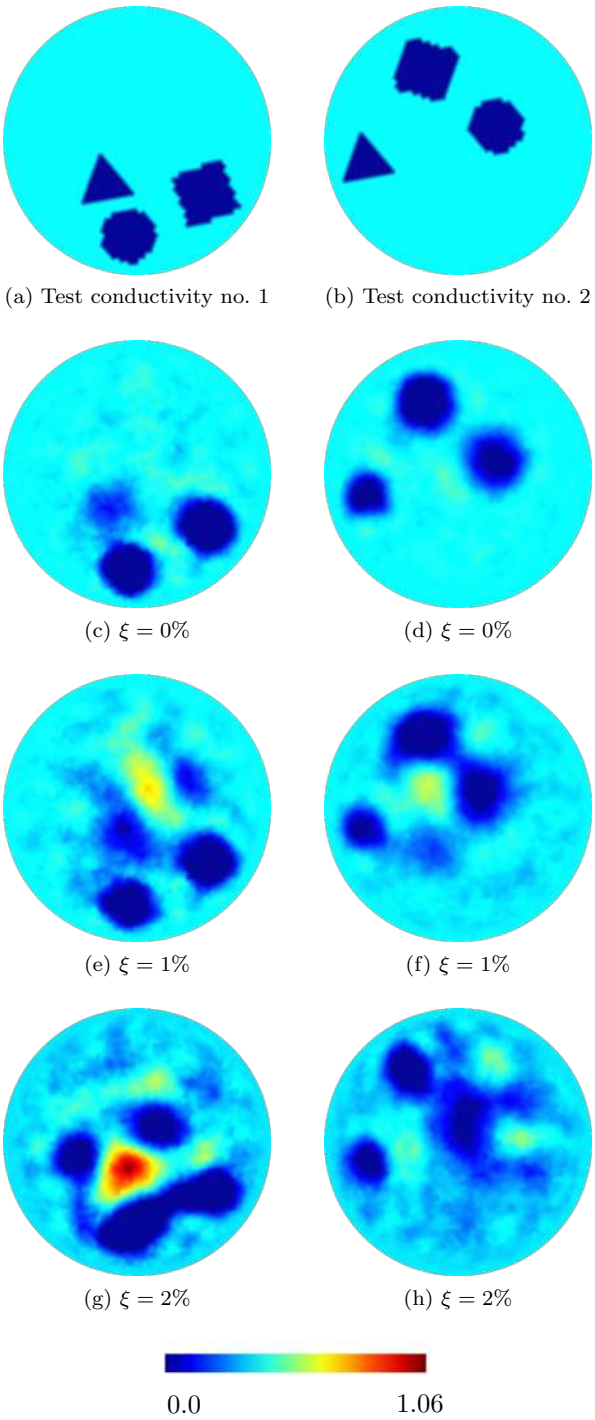

(a) Test conductivity no. 1 (b) Test conductivity no. 2

(c) $\xi = 0\%$ (d) $\xi = 0\%$

(e) $\xi = 1\%$ (f) $\xi = 1\%$

(g) $\xi = 2\%$ (h) $\xi = 2\%$

Fig. 7. Comparison between the real conductivity distribution of first two test samples (top row) and the conductivity distribution obtained by CNN for noisy data with 0, 1 and 2% error (second, third and last rows, respectively.)

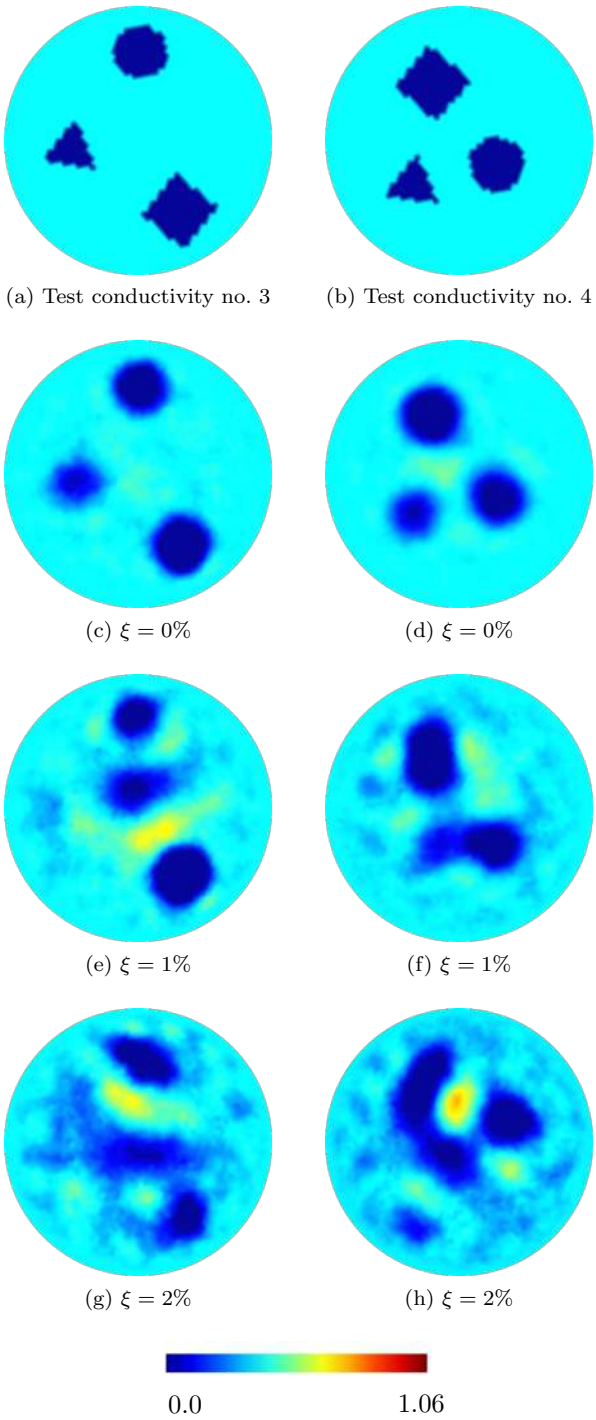

(a) Test conductivity no. 3 (b) Test conductivity no. 4

(c) $\xi = 0\%$ (d) $\xi = 0\%$

(e) $\xi = 1\%$ (f) $\xi = 1\%$

(g) $\xi = 2\%$ (h) $\xi = 2\%$

Fig. 8. Comparison between the real conductivity distribution of last two test samples (top row) and the conductivity distribution obtained by CNN for noisy data with 0, 1 and 2% error (second, third and last rows, respectively.)

effects are usually small and can be neglected. However, for a better quality reconstruction, the capacitive effect must be considered (Martins and Tsuzuki, 2017).

Future research may include incorrect electrode placement and irregular contour geometry.

ACKNOWLEDGEMENTS

A. K. Sato is supported by FUSP/Petrobras. G. C. Duran and M. S. G. Tsuzuki are supported by CNPq (Grants 140.299/2020–3 and 311195/2019–9). The paper has the support from CAPES/PROAP - Grant 817.757/38.860.

REFERENCES

Alsaker, M. and Mueller, J.L. (2018). Use of an optimized spatial prior in D-bar reconstructions of EIT tank data. *Inverse Probl Imag*, 12(4), 883–901.

Bianchessi, A., Akamine, R.H., Duran, G.C., Tanabi, N., Sato, A.K., Martins, T.C., and Tsuzuki, M.S.G. (2020). Electrical impedance tomography image reconstruction based on neural networks. *IFAC-PapersOnLine*, 53(2), 15946–15951.

Duran, G.C., Sato, A.K., Tanabi, N., Nasiri, H., Takimoto, R.Y., Barari, A., Martins, T.C., and Tsuzuki, M.S.G. (2021). Framework for electrical impedance tomography forward problem with non-uniform electrodes distribution. In L.Y. Cheng (ed.), *ICGG 2020 - Proceedings of the 19th International Conference on Geometry and Graphics*, 320–331. Springer International Publishing, Cham.

Geuzaine, C. and Remacle, J.F. (2009). Gmsh: A 3-D finite element mesh generator with built-in pre- and post-processing facilities. *Int J Numer Meth Eng*, 79(11), 1309–1331.

Hamilton, S.J. and Hauptmann, A. (2018). Deep d-bar: Real-time electrical impedance tomography imaging with deep neural networks. *IEEE Transactions on Medical Imaging*, 37(10), 2367–2377.

Krizhevsky, A., Sutskever, I., and Hinton, G. (2012). Imagenet classification with deep convolutional neural networks. *Neu Inf Pro Syst*, 25.

Lecun, Y., Bottou, L., Bengio, Y., and Haffner, P. (1998). Gradient-based learning applied to document recognition. *Proc IEEE*, 86(11), 2278–2324.

Lymperopoulos, G., Lymperopoulos, P., Alikari, V., Dafogianni, C., Zyga, S., and Margari, N. (2017). Applications for electrical impedance tomography (eit) and electrical properties of the human body. In P. Vlamos (ed.), *GeNeDis 2016*, 109–117. Springer International Publishing, Cham.

Martins, T.C., Camargo, E.D.L.B., Lima, R.G., Amato, M.B.P., and Tsuzuki, M.S.G. (2011). Electrical impedance tomography reconstruction through simulated annealing with incomplete evaluation of the objective function. In *33rd IEEE EBMS*, 7033–7036. Boston, USA.

Martins, T.C. and Tsuzuki, M.S.G. (2011). Simulated annealing with partial evaluation of objective function applied to electrical impedance tomography. *IFAC Proceedings Volumes*, 44(1), 4989–4994.

Martins, T.C. and Tsuzuki, M.S.G. (2012). Electrical impedance tomography reconstruction through simulated annealing with total least square error as objective function. In *34th IEEE EMBC*, 1518–1521. San Diego, USA.

Martins, T.C. and Tsuzuki, M.S.G. (2013). Electrical impedance tomography reconstruction through simulated annealing with multi-stage partially evaluated objective functions. In *35th IEEE EMBC*, 6425–6428. Osaka, Japan.

Martins, T.C. and Tsuzuki, M.S.G. (2015). EIT image regularization by a new multi-objective simulated annealing algorithm. In *Proc 37th IEEE EMBC*, 4069–4072. Milan, Italy.

Martins, T.C., Fernandes, A.V., and Tsuzuki, M.S.G. (2014). Image reconstruction by electrical impedance tomography using multi-objective simulated annealing. In *IEEE 11th ISBI*, 185–188. Beijing, China.

Martins, T.C. and Tsuzuki, M.S.G. (2017). Investigating Anisotropic EIT with Simulated Annealing. *IFAC-PapersOnLine*, 50(1), 9961–9966.

Sato, A.K., Bianchessi, A., Martins, T.C., Lima, R.G., and Tsuzuki, M.S.G. (2018). A new 2D dual layered electrode model for the electrical impedance tomography. *IFAC-PapersOnLine*, 51, 41–46.

Silva, O.L., Lima, R.G., Martins, T.C., Moura, F.S., Tavares, R.S., and Tsuzuki, M.S.G. (2017). Influence of current injection pattern and electric potential measurement strategies in electrical impedance tomography. *Control Eng Pract*, 58, 276–286.

Tan, C., Lv, S., Dong, F., and Takei, M. (2018). Image reconstruction based on convolutional neural network for electrical resistance tomography. *IEEE Sensors Journal*, 19(1), 196–204.

Tavares, R.S., Martins, T.C., and Tsuzuki, M.S.G. (2012). Electrical impedance tomography reconstruction through simulated annealing using a new outside-in heuristic and GPU parallelization. *Journal of Physics: Conference Series*, 407, 012015.

Tavares, R.S., Nakadaira-Filho, F.A., Tsuzuki, M.S.G., Martins, T.C., and Lima, R.G. (2014). Discretization error and the EIT forward problem. *IFAC-PapersOnLine*, 47(3), 7535–7540.

Tavares, R.S., Tsuzuki, M.S.G., Martins, T.C., and Lima, R.G. (2015). The EIT forward problem parallelized using a colored pJDS matrix format. *IFAC-PapersOnLine*, 48(20), 42–47.

Teschner, E., Imhoff, M., and Leonhardt, S. (2015). *Electrical Impedance Tomography: The realisation of regional ventilation Monitoring, 2nd edition.*

Trigo, F., Gonzalez Lima, R., and Amato, M. (2004). Electrical impedance tomography using the extended kalman filter. *IEEE Transactions on Biomedical Engineering*, 51(1), 72–81.